Research Article | Open Access

Microstructures

Wei *et al. Microstructures* **2026**, *6*, 20260119 **DOI:**10.20517/microstructures.2025.161

Improving osseointegration and antibacterial ability of Nb-doped micro arc oxidized coating with rod-like hydroxyapatite crystals on titanium surface

Daqing Wei[1], Qing Du[2,3], Yuri V. Petrov[5], Qingyu Wang[1], Su Cheng[3], Yaming Wang[4]

Keywords:
Micro arc oxidation, Nb element, microwave hydrothermal treatment, osseointegration, antibacterial ability

Citation: Wei, D.; Du, Q.; Petrov, Y. V.; Wang, Q.; Cheng, S.; Wang, Y. Improving osseointegration and antibacterial ability of Nb-doped micro arc oxidized coating with rod-like hydroxyapatite crystals on titanium surface. *Microstructures* **2026**, *6*, 20260119. https://dx.doi.org/10.20517/microstructures.2025.161

Received: 29 Nov 2025 **First Decision:** 14 Jan 2026 **Revised:** 5 Feb 2026 **Accepted:** 24 Mar 2026 **Published:** 8 Sep 2026

Academic Editor: Yuxiao Lai
Copy Editor: Fangling Lan
Production Editor: Fangling Lan

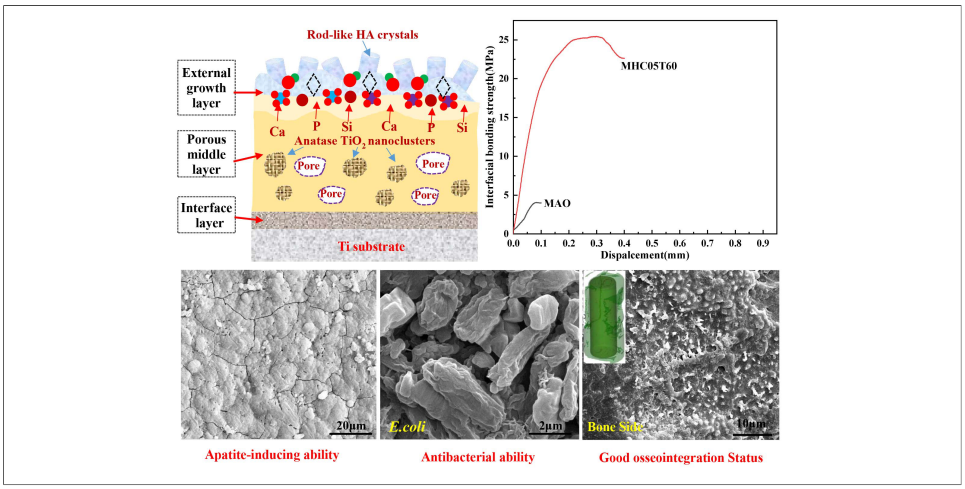

Abstract

A niobium (Nb)-doped micro arc oxidized coating (MAO) was fabricated on a titanium substrate, and microwave hydrothermal (MH) post-treatment was applied to regulate the microstructure of the coating, aiming to enhance bone-implant osseointegration and antibacterial performance. The experimental results showed that the as-prepared MAO coating was composed of nanocrystalline TiO_2 and a large amount of amorphous phase containing oxygen, Nb, calcium, phosphorus, and other bioactive elements. After MH treatment, short rod-like hydroxyapatite (HA) crystals were uniformly formed on the porous surface of the Nb-doped MAO coating, resulting in a well-ordered crystalline structure with tight interfacial bonding between the HA crystals and the MAO coating. The incorporation of Nb and MH post-treatment synergistically optimized the surface microtopography and chemical composition of the MAO coating, which markedly enhanced *in vitro* bioactivity, *in vivo* osseointegration, and antibacterial properties.

[1]College of Nuclear Science and Technology, Harbin Engineering University, Harbin 150001, Heilongjiang, China.
[2]Center for Biomedical Materials and Engineering, Harbin Engineering University, Harbin 150001, Heilongjiang, China.
[3]Department of Civil Engineering, School of Architecture and Civil Engineering, Harbin University of Science and Technology, Harbin 150001, Heilongjiang, China.
[4]Department of Materials Science and Engineering, Harbin Institute of Technology, Harbin 150001, Heilongjiang, China.
[5]Laboratory of Dynamics and Extreme Characteristics of Promising Nanostructured Materials, Saint Petersburg State University, St. Petersburg 199034, Russia.

Correspondence to: Dr. Qing Du, Department of Civil Engineering, School of Architecture and Civil Engineering, Harbin University of Science and Technology, No. 52 Xuefu road, Harbin, Harbin 150001, Heilongjiang, China. E-mail: duqing@hrbust.edu.cn; Dr. Qingyu Wang, College of Nuclear Science and Technology, Harbin Engineering University, Harbin 150001, Heilongjiang, China. E-mail: wangqingyu@hrbeu.edu.cn

INTRODUCTION

Titanium (Ti) and its alloys have been widely applied in the biomedical field as key materials for hard tissue replacement[1], and are commonly used in dental implants, orthopedic prostheses, and fracture fixation devices, owing to three main attributes[1-3]: excellent biocompatibility, favorable mechanical properties, and outstanding *in vivo* corrosion resistance. However, these materials still exhibit notable limitations when used as hard tissue substitutes. For instance, dental root implants require rapid osseointegration, defined as the formation of a stable biomechanical bond with human alveolar bone[4-6]. This requirement contrasts with the inherent biological inertness of titanium, which limits direct chemical bonding with living tissue. Clinically, this surface bio-inertness results in insufficient bone-implant interfacial integration. Specifically, titanium surfaces lack osteoinductive properties to stimulate bone tissue regeneration, thereby hindering the formation of a functional osteophilic interface essential for long-term implant stability[4].

A promising approach to form a bone-bonding interface involves the application of bioactive coatings on titanium surfaces[7-9]. Numerous studies have investigated the fabrication of bioactive coatings using various surface treatment methods, including plasma spraying, sol-gel processing, magnetron sputtering, laser cladding, and electrochemical deposition[10-14]. These methods represent a broad range of surface coating techniques. However, several challenges remain, including insufficient adhesion strength between the coating and substrate, high processing cost, and complicated procedures. Furthermore, the complex surface topography of threaded implants complicates the formation of uniform coatings[12,13]. In addition, some coated implants tend to induce inflammatory reactions in surrounding tissues after implantation, which further limits the clinical application of Ti-based implant materials[15].

Microarc oxidation (MAO) coatings are a promising surface modification technology for Ti and its alloys[16,17]. This method overcomes the limitations of conventional coating preparation techniques and offers four distinct advantages. First, the MAO coating is formed by *in situ* oxidation of the Ti substrate, producing a metallurgical bonding interface with high bonding strength. Second, the preparation process is simple, low-cost, and time-efficient, and the entire oxidation process can be completed within a few minutes. Third, MAO technology shows strong adaptability to substrates with complex geometries and can form uniform porous coatings on threaded or porous implants. Fourth, the chemical composition and microtopography of the MAO coating can be tailored by adjusting the electrolyte composition and oxidation parameters. Early MAO coatings were mainly composed of titanium oxides[18-20]. With further research development, Ca and P elements were incorporated into MAO coatings to improve biological activity[21-23]. However, these bioactive elements are mainly distributed in the amorphous phase of MAO coatings, which limits their osteoinductive potential and results in only limited improvement in coating bioactivity.

To further enhance the biological performance of MAO coatings, various post-treatment methods have been developed[21-23], such as heat treatment, conventional hydrothermal treatment, and chemical treatment[17,23-28]. Nevertheless, these post-treatment methods have inherent limitations. Heat treatment is difficult to induce the formation of a bioactive hydroxyapatite (HA) phase in the MAO coating[29]. Chemical treatments (NaOH solution soaking) can improve the bioactivity of MAO coatings but cannot form stable HA crystals, and prolonged treatment may damage the coating-substrate interface and reduce the mechanical properties of the coating[17,29]. Conventional hydrothermal treatment can induce HA phase formation, but the treatment time is long and crystal morphology is difficult to control[21-23]. Microwave hydrothermal (MH) treatment is a novel and efficient post-treatment technique for MAO coatings[29-31]. This method combines the advantages of microwave heating and hydrothermal reaction, enabling rapid formation of HA crystals while maintaining the bonding strength of the coating-substrate interface[31]. However, most HA crystals formed by conventional MH treatment are nanowires or long rod-like structures, and it remains difficult to obtain uniform short rod-like HA crystals that closely resemble the natural HA morphology in human bone[29-31].

Table 1. Composition of the electrolyte for MAO treatment

Chemical reagent	Concentration ($g \cdot L^{-1}$)
EDTA-2Na	15.0
$Ca(CH_3COO)_2 \cdot H_2O$	8.80
$Ca(H_2PO_4)_2 \cdot H_2O$	6.30
$Na_2SiO_3 \cdot 9H_2O$	7.10
$C_{10}H_5NbO_{20}$	5.00
NaOH	5.00
H_2O_2	6.00

In addition to insufficient osseointegration, bacterial infection is another major factor leading to implant failure in clinical practice[4]. To address this issue, various strategies have been explored to impart antibacterial properties to MAO coatings. Zhang *et al.*[32] introduced silver nanoparticles into the MAO coating to enhance antibacterial capacity, and the antibacterial effect increased with increasing silver ion doping concentration. Zhou *et al.*[33] prepared MAO coatings modified with HA nanodot arrays and loaded ciprofloxacin-loaded chitosan hydrogel in specific regions to achieve a synergistic effect of osseointegration and antibacterial performance. Wu *et al.*[34] fabricated an antibacterial coating by loading halogenated furanone compound-loaded poly (L-lactic acid) nanoparticles on the Ti surface. In addition, doping trace metal elements, such as Cu[35], Zn[36], and Sr[37] into MAO coatings is a simple and effective method to regulate antibacterial activity. Nb is a biocompatible metal element with osteogenic promotion ability and antibacterial potential, and its incorporation into MAO coatings is expected to synergistically enhance both osseointegration and antibacterial properties.

In this study, Nb was doped into the MAO coating by adding Nb-containing compounds to the electrolyte, followed by MH post-treatment to regulate the surface microstructure of the Nb-doped MAO coating. The effects of Nb doping and MH treatment on microstructure, phase composition, *in vitro* bioactivity, antibacterial performance, and *in vivo* osseointegration of the MAO coating were systematically investigated. The formation mechanism of short rod-like HA crystals on the Nb-doped MAO coating during MH treatment was further clarified, and a multifunctional Ti-based implant surface with enhanced osseointegration and antibacterial performance was developed. This approach provides a new strategy for the surface modification of dental and orthopedic implants.

MATERIALS AND METHODS

MAO treatment

Ti sheets (10 × 10 × 1 mm^3) and Ti rods (Φ2 × 6 mm^3) were used as substrate materials, and all specimens were pretreated to remove the oxide layer and surface contaminants. First, the Ti samples were degreased by ultrasonic cleaning in acetone solution for 30 min to eliminate surface oil. Then, the Ti samples were wet-polished using SiC sandpaper with progressively finer grits (#600, #800, #1200, and #2000) until the surface was smooth with no visible scratches. After polishing, the samples were sequentially ultrasonically cleaned in acetone, deionized water, and 75% medical ethanol for 30 min each, and finally dried in a constant-temperature oven at 30 °C for subsequent MAO treatment.

The MAO experiment was conducted in a specialized electrolyte cell, with Ti samples as the anode and stainless steel as the cathode. The electrolyte composition is presented in Table 1, and the electrolyte was continuously stirred during the oxidation process to maintain uniform temperature and composition. All reagents were purchased from Harbin Yanjie Technology Co., Ltd. The key MAO parameters were set as follows: applied voltage of 400 V, pulse frequency of 600 Hz, duty cycle of 8%, and oxidation time of 5 min.

Table 2. Sample labels and corresponding MH treatment parameters

Sample	NaOH (mol/L)	Temperature (°C)	Microwave power (W)	Time (min)
MHC05T10	0.5	200	800	10
MHC05T60	0.5	200	800	60

MH: Microwave hydrothermal.

Microwave hydrothermal post-treatment

The MAO-treated samples were subjected to MH post-treatment using an MH synthesis instrument (XH-800s, China). The samples were fixed in a hydrothermal reactor kettle and completely immersed in 0.5 mol/L NaOH solution. The MH treatment parameters were set as a temperature of 200 °C, microwave power of 800 W, and treatment times of 10 and 60 min, respectively. The detailed treatment procedures have been reported in previous studies[29-31]. After the MH reaction, the samples were immediately removed, soaked in deionized water for 10 min to remove residual alkali, and dried in an oven at 30 °C for 2 h. For convenience of description, the samples were labelled as shown in Table 2.

Simulated body fluid immersion

The apatite-inducing ability of the samples was evaluated by soaking in simulated body fluid (SBF)[38]. The samples were immersed in 30 mL of SBF solution, and the SBF was refreshed every 48 h to maintain a stable ion concentration. The soaking time was set to 3, 5, and 7 days, and the experiment was conducted in a constant-temperature incubator at 37 °C. The SBF solution was prepared by dissolving analytical-grade NaCl (8.030 g/L), $NaHCO_3$ (0.352 g/L), KCl (0.225 g/L), $K_2HPO_4{\cdot}3H_2O$ (0.230 g/L), $MgCl_2{\cdot}6H_2O$ (0.311 g/L), $CaCl_2$ (0.293 g/L), and Na_2SO_4 (0.0720 g/L) in deionized water. The pH value of the solution was adjusted to 7.4 using 6.06 g/L Tris hydroxymethylaminomethane ($(CH_2OH)_3CNH_2$) and 1 mol/L HCl. All reagents were purchased from Harbin Yanjie Technology Co., Ltd.

Structure characterization

X-ray diffraction

X-ray diffraction (XRD) analysis was performed using a D/max-γB X-ray diffractometer (Japan) with CuKα radiation to characterize the phase composition of the samples. The test parameters were set as follows: accelerating voltage of 40 kV, current of 40 mA, scanning range from 10° to 90°, and scanning rate of 10°/min. The phase composition was identified by comparison with the standard PDF card database.

Scanning electron microscopy (SEM) and energy dispersive X-ray spectrometer (EDS)

The surface microtopography of the samples was observed using a Helios Nanolab 600i scanning electron microscope (SEM, FEI Co., USA) at an accelerating voltage of 20 kV. The elemental composition of the samples was analyzed using an energy dispersive X-ray spectrometer (EDS, Oxford, UK) integrated with the SEM system.

Focused ion beam (FIB) and transmission electron microscopy (TEM)

Transmission electron microscopy (TEM, Talos F200x, FEI Co., USA) was used to characterize the fine microstructure and crystal structure of MHC05T60 samples at an accelerating voltage of 200 kV. The TEM samples were prepared using a focused ion beam (FIB, Helios Nanolab 600i, FEI Co., USA) to ensure appropriate thickness and structural integrity. High-resolution TEM (HRTEM) and fast Fourier transform (FFT) were used to analyze the crystal phase. Elemental mapping and line scanning were performed using the EDS system integrated with the TEM system.

In vitro antibacterial test

The antibacterial performance of the samples was evaluated using *Escherichia coli* (*E. coli,* Gram-negative) and *Staphylococcus aureus* (*S. aureus,* Gram-positive), which are the main pathogenic bacteria causing implant-related infections. The cultivation procedures for *E. coli* and *S. aureus* have been reported in previous studies[20,39]. First, the bacterial strains were inoculated onto solid bacterial media and cultured at 37 °C for 24 h. Subsequently, the cultures were transferred to fresh solid media every 24 h. After two rounds of solid-phase cultivation, a small aliquot of viable bacteria was transferred to liquid bacterial media and incubated at 37 °C for an additional 24 h. The bacterial suspension was diluted with phosphate-buffered saline (PBS) to a concentration of 1.75×10^5 cfu/mL for subsequent experiments.

The samples were placed in a 24-well plate and sterilized using an autoclave at 121 °C for 30 min after a 2 h immersion in 70 v/v% ethanol within a sterile culture hood. Then, 1 mL of the bacterial suspension was added to each well and incubated at 37 °C for 24 h without shaking. Subsequently, bacteria at a concentration of 1.75×10^5 cfu/mL were seeded onto the samples, and the samples were placed back into the 24-well plate and incubated at 37 °C for 24 h. After incubation, the samples were rinsed with PBS to remove non-adhered bacteria, and the adhered bacteria were eluted by ultrasonic vibration for 5 min. The eluent was diluted to an appropriate concentration, spread on solid LB agar medium, and cultured at 37 °C for 24 h. The number of bacterial colonies was counted under an optical microscope, and the antibacterial rate (R) was calculated according to Equation (1):

$$R = (A - B)/A^*100\% \quad (1)$$

where A is the number of bacterial colonies for the blank group, and B is the number of bacterial colonies for the MAO and MHC05T60 samples.

In addition, the morphology of adhered bacteria on the sample surface was observed by SEM to further evaluate the antibacterial effect. The samples with adhered bacteria were fixed with 2.5% glutaraldehyde solution for 4 h, dehydrated using a gradient ethanol series (30%, 50%, 70%, 80%, 90%, 95%, 100%), and then dried and sputtered with gold for SEM observation.

Electrochemical corrosion experiment

The electrochemical corrosion behavior of MAO and MAO-Nb coatings was evaluated using a Reference 600 electrochemical workstation (Gammry, USA) in 0.5 mol/L NaOH solution. A conventional three-electrode system was adopted: the sample, with an exposed area of 0.3 cm^2, served as the working electrode, a platinum plate acted as the auxiliary electrode, and a saturated calomel electrode (SCE) was used as the reference electrode. Before the test, the sample was immersed in the electrolyte for 5 min to reach a stable open-circuit potential (OCP).

Potentiodynamic polarization curves were measured in the potential range from +1 V to -1 V (*vs.* SCE) with a scanning rate of 1 $mV \cdot s^{-1}$, and the corrosion potential (E_{corr}), corrosion current density (I_{corr}), and polarization resistance (R_p) were obtained by fitting the polarization curves using Gamry Echem Analyst software. Electrochemical impedance spectroscopy (EIS) was performed in the frequency range of 10^{-2} Hz to 10^5 Hz with an alternating current amplitude of 10 mV, and the EIS data were fitted and analyzed using ZSimpWin software to determine the impedance parameters of the coating.

In vivo osseointegration test

Animal experimental models

The tibial implantation model was covered by the approved animal protocol (IACUC No. 2020127). A total of 28 healthy and mature New Zealand rabbits (half male and half female, body weight of 2.5-3.0 kg) were obtained from Wanle Domestic Rabbit Breeding Base and randomly divided into two groups (MAO group and MHC05T60 group), with 14 rabbits in each group.

The detailed implantation procedure is described as follows[29-31]. The rabbits were anesthetized by ear vein injection of 3% pentobarbital sodium solution (30 mg/kg body weight). The hair around the midpoint of the rabbit tibia was shaved, and the skin was disinfected with 2% iodophor and 75% alcohol. A local anesthetic (2% lidocaine) was injected subcutaneously, and a longitudinal incision of about 1.5 cm was made to expose the tibial cortical bone by cutting the skin, fascia, and periosteum. A cylindrical hole with a size of Φ2 × 6 mm^3 was drilled into the tibia using a dental drill under continuous saline cooling to avoid damage to the bone tissue. The MAO and MHC05T60 implants were inserted into the bone holes, and the periosteum, fascia, and skin were sutured layer by layer. After implantation, the rabbits were intramuscularly injected with gentamicin (1 mL/day) for 3 consecutive days to prevent infection and were housed in a clean animal room with free access to food and water. The surgical sutures were removed 10 days after implantation.

Implant retrieval

At 4 and 8 weeks after implantation, 7 rabbits in each group were euthanized by ear vein injection of air, and the tibial segments containing the implants were immediately excised. The residual soft tissue on the tibial surface was carefully removed using surgical scissors, and the samples were rinsed with normal saline for subsequent characterization. After implant retrieval, the microstructures of both the tibia side and the implant side were examined using a Helios Nanolab 600i scanning electron microscope (SEM, FEI Co., USA) to evaluate the tissue response around the implant.

Radiographic evaluation

X-ray digital radiography (Ultral Focus100, Faxitron X-Ray, USA) was used to observe the bone-implant interface at 4 and 8 weeks after implantation, and the presence of bone resorption, gaps, and implant loosening was evaluated. Micro-CT (Siemens, USA) was used for three-dimensional reconstruction of the implant-bone complex. The scanning parameters were set as follows: voltage of 80 kV, current of 100 μA, scanning rate of 6°/min, and spatial resolution of 9 μm. Inveon Research Workplace V6 (IRWV6, Siemens, USA) software was used to analyze the micro-CT data, and bone volume/total volume (BV/TV) and bone surface/total volume (BS/TV) of the bone tissue within 500 μm around the implant were calculated to quantify new bone formation.

SEM observation of the bone-implant interface

The tibial segments containing implants were fixed with 4% paraformaldehyde solution for 24 h, and the implants were then carefully separated from the bone tissue. The surfaces of the implant and the bone tissue at the interface were observed by SEM, and EDS analysis was performed to characterize the elemental composition at the interface in order to evaluate the bonding status between the implant and the surrounding bone tissue.

Statistical analysis

All experimental data were expressed as mean ± standard deviation ($x \pm s$), and statistical analysis was performed using SAS 6.0 software. One-way analysis of variance (ANOV$\overline{A}$) was used to compare differences between groups, and $P < 0.05$ was considered statistically significant. All *in vitro* experiments and surface

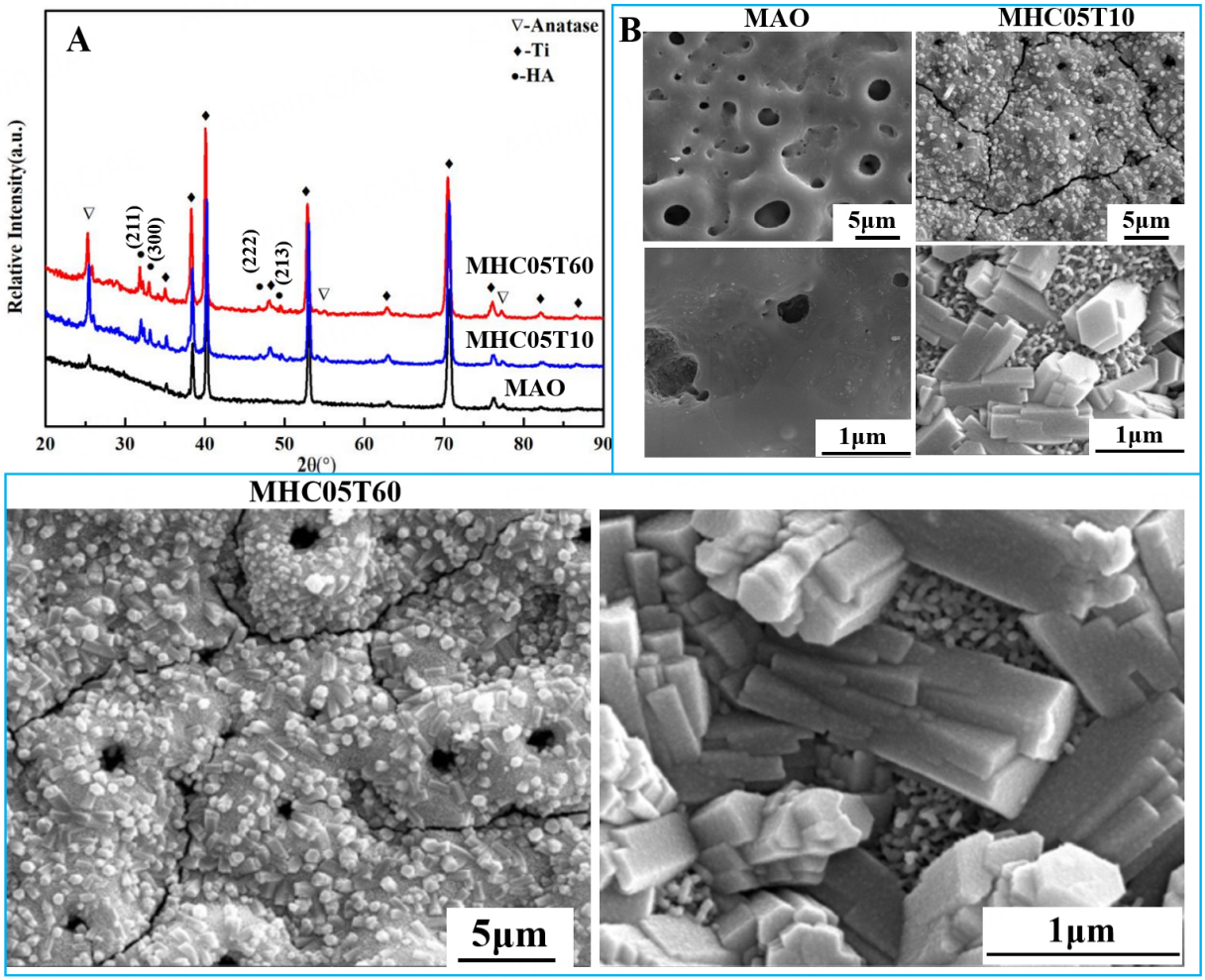

Figure 1. XRD patterns (A) and SEM images (B) of MAO, MHC05T10 and MHC05T60 samples.

characterizations were repeated at least three times to ensure reproducibility of the results. OriginPro 2018C and Microsoft Office 2024 were used to generate the experimental figures and tables.

RESULTS

XRD analysis and SEM images of MHC05T10 and MHC05T60 samples

The phase composition and surface microstructure of MAO, MHC05T10, and MHC05T60 samples were characterized by XRD and SEM, and the results are shown in Figure 1. As observed from the XRD patterns [Figure 1A], the MAO sample mainly exhibits diffraction peaks of the Ti substrate and a weak anatase TiO_2 peak, and no obvious HA phase diffraction peak is detected, indicating that the MAO coating is primarily composed of an amorphous structure and anatase TiO_2 phase. After MH treatment, the diffraction intensity of anatase TiO_2 in the MHC05T10 and MHC05T60 samples is significantly enhanced, and new diffraction peaks appear at 2θ = 31.9°, 33.1°, 46.7°, and 49.5°, which correspond to the (211), (300), (222), and (213) crystal planes of the HA phase (PDF: 73-0294), indicating that MH treatment can induce the formation of HA crystals on the Nb-doped MAO coating. With increasing MH treatment time, the diffraction intensity of HA phase peaks in the MHC05T60 sample is higher than that in the MHC05T10 sample, indicating that the content of HA crystals increases with prolonged treatment time.

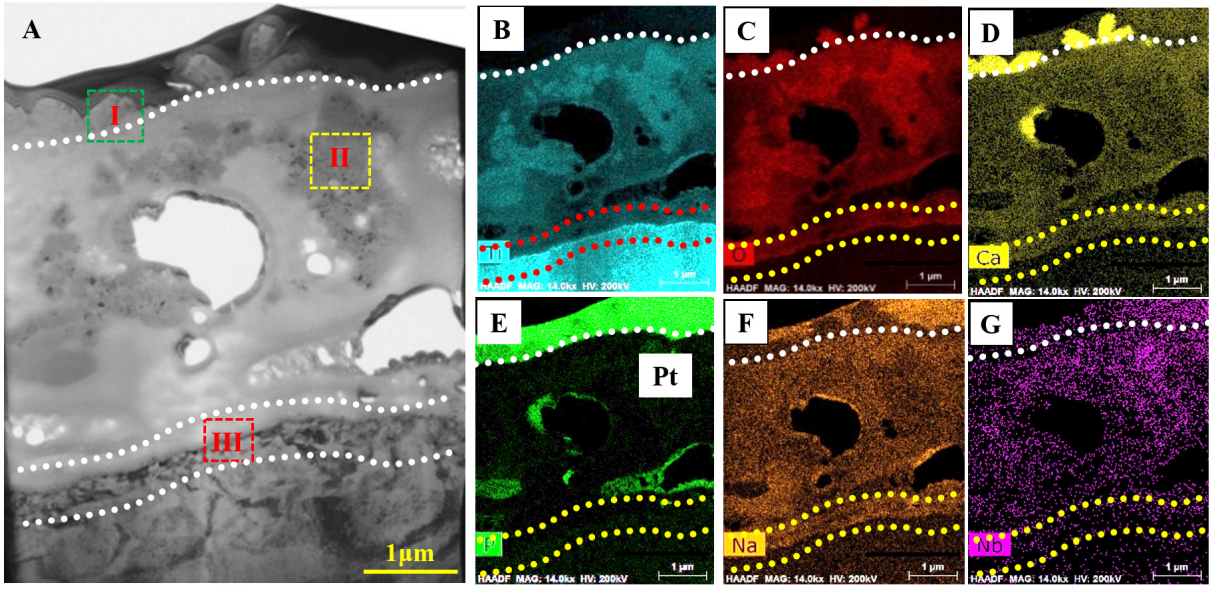

Figure 2. TEM image and EDS map-scanning images of the cross-sectional MHC05T60 sample: (A) TEM bright field image; (B) Ti element; (C) O element; (D) Ca element; (E) P element; (F) Na element; (G) Nb element.

Figure 1B presents SEM images of MAO, MHC05T10, and MHC05T60 samples. The MAO sample exhibits a typical porous surface with microscale dimensions, with pore sizes ranging from several micrometres to tens of micrometres, and the pore surface appears relatively smooth. After MH treatment, the MHC05T10 and MHC05T60 samples continue to exhibit a porous structure, with numerous short rod-like HA crystals observed on their surfaces. Magnified SEM images indicate that these crystals form a well-ordered HA submicron pillar structure on the MAO coatings, and the crystals are densely arranged. The length of the short rod-like HA crystals in the MHC05T60 sample is slightly greater than that in the MHC05T10 sample, which is consistent with the XRD analysis results, indicating that the growth of HA crystals is promoted with increasing MH treatment time.

Microstructure analysis of the cross-sectional MHC05T60 coating

To further investigate the microstructure and elemental distribution of the MHC05T60 sample, the results are shown in Figures 2-4. The cross-sectional TEM image in Figure 2A clearly shows that the MHC05T60 coating exhibits a typical three-layer structure: (I) an outermost growth layer with short rod-like HA crystals, (II) a middle porous layer containing anatase TiO_2 clusters and an amorphous structure, and (III) an interface layer with TiO_2 nanocrystals. In region I, Ca, P, and O elements are mainly concentrated in the outermost growth layer [Figures 2C-E]. In contrast, the middle porous region (region II) exhibits lower concentrations of Ca and P, with uneven distributions of Ca, P, Na, and Nb elements [Figures 2D-G]. Additionally, several nanocrystal clusters with higher concentrations of Ti and O elements are observed in the middle porous region, and similar features are present in adjacent regions of the porous layer [Figures 2B and C]. Furthermore, in region III, the boundary between the porous layer and the Ti substrate exhibits a strong bonding interface.

The magnified TEM image, along with the corresponding HRTEM and FFT images of regions II and III presented in Figure 2A, is shown in Figure 3. The magnified TEM image [Figure 3A] reveals that the average size of the crystal clusters in region II is about 50 nm. The HRTEM and FFT patterns [Figures 3B and C] show that the lattice fringes with d-spacings of 0.243 and 0.342 nm correspond to the (103) and (202) crystal planes of anatase, and the FFT pattern exhibits typical diffraction spots of anatase TiO_2 along the [010] zone

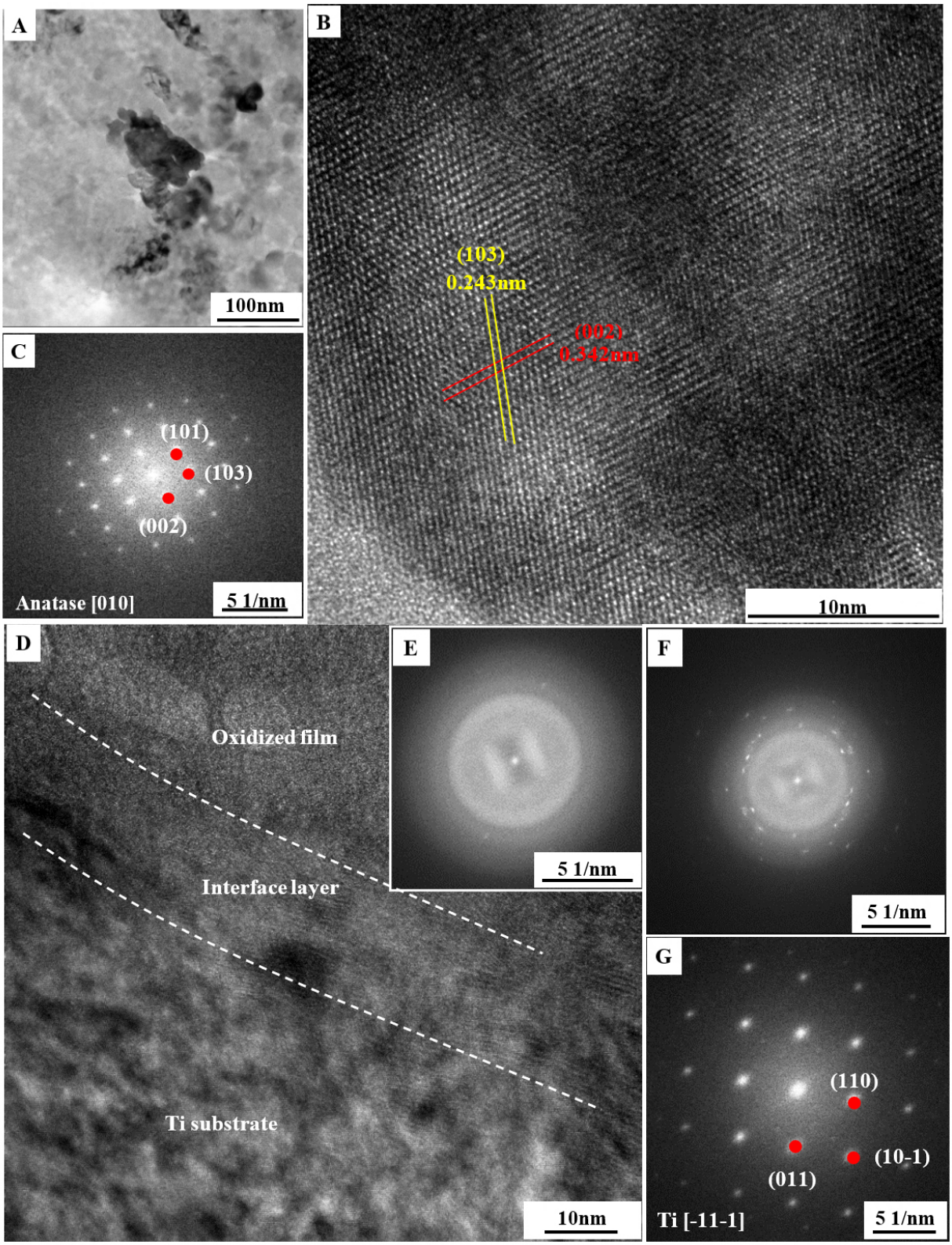

Figure 3. TEM magnified image, HRTEM image and FFT image of region I and region II in the Figure 2A: (A-C) magnified TEM image, HRTEM and FFT images of region II; (D-G) Magnified TEM image and FFT images of region III.

axis [Figures 3B and C], indicating that the nanocrystalline clusters are anatase. The magnified TEM image further indicates that region III comprises an oxidized layer, an interface layer, and the Ti substrate, and the

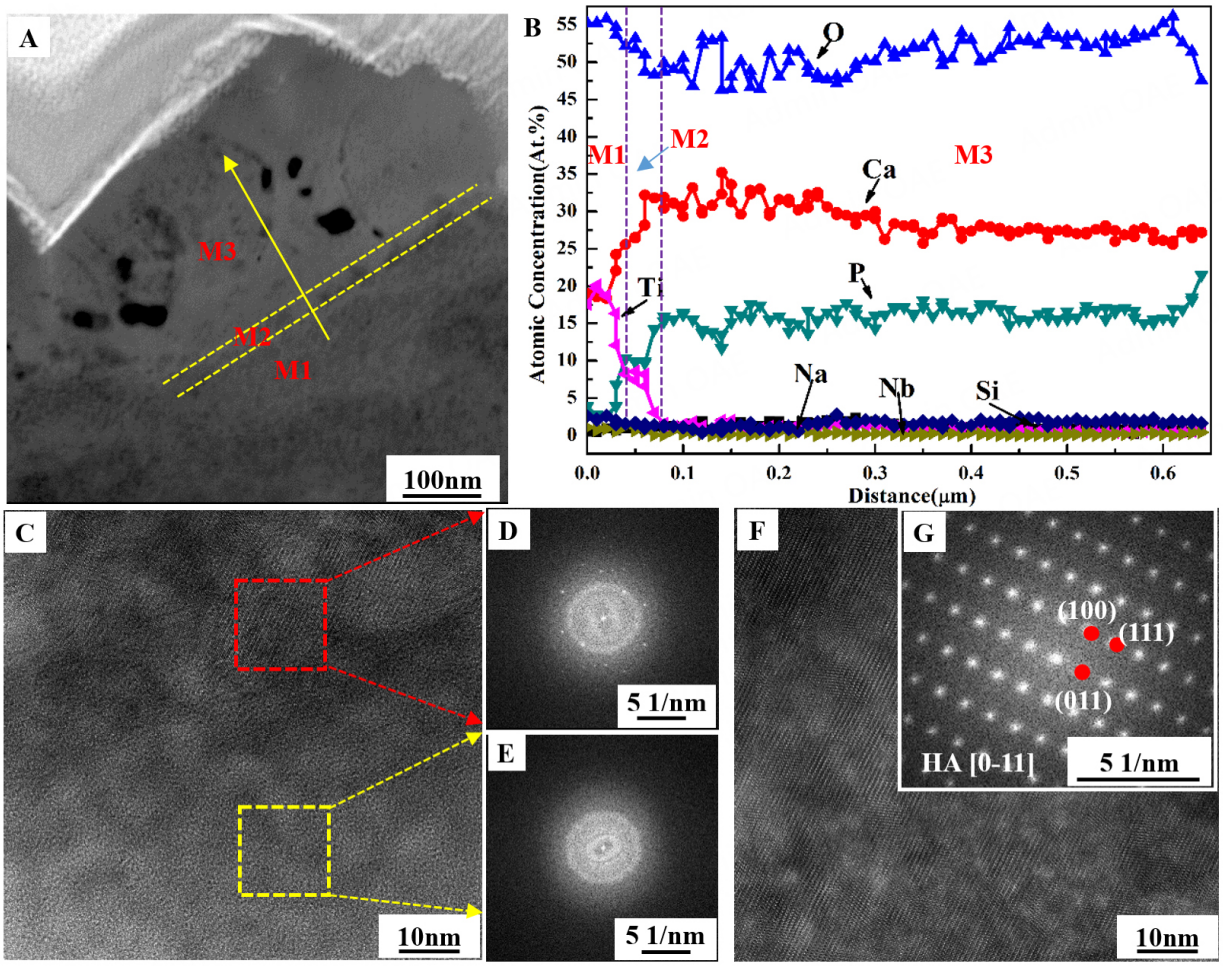

Figure 4. TEM magnified image, EDS image, HRTEM images and FFT images of region I in Figure 2A. (A) Magnified TEM image; (B) The EDS lining scanning image; (C-E) HRTEM image and FFT images of area M1 and M2; (F and G) HRTEM image and FFT images of area M1.

lattice fringes of the Ti substrate correspond to the (110), (10-1), and (011) crystal planes of Ti with the [-11-1] zone axis, as shown in Figures 3D-G. The metallurgical bonding between the interface layer and the Ti substrate is tight, without obvious gaps, which ensures high bonding strength of the coating.

The magnified TEM image and EDS line-scanning results of the outermost growth layer of the MHC05T60 coating are shown in Figure 4. The EDS line-scanning results [Figure 4B] show that the outermost layer can be divided into three typical regions: areas M1, M2, and M3. In area M1, the main elemental compositions are 20 at% Ti, 55 at% O, 20 at% Ca, and 2.5 at% P and 2.5 at% Na, while the atomic concentrations of Si and Nb are nearly zero. In area M2, the atomic concentrations of Ti and O decrease significantly to 7.5 at% and 47.5 at%, respectively, whereas those of Ca and P increase notably to 27.5 at% and 10 at%, respectively. The contents of Si, Nb, and Na are about 2.5 at% each. In area M3, the main elemental compositions are Ca, P, and O, along with small amounts of Si and Nb, with concentrations of 30 at%, 15 at%, 50 at%, 2.5 at%, and 2.5 at%, respectively. The HRTEM and FFT results show that area M1 exhibits an amorphous structure [Figures 4C and E], region M2 contains a polycrystalline HA phase [Figure 4C and D], and region M3 consists of a single HA phase with the [0-11] zone axis [Figures 4F and G], indicating that the outermost growth layer exhibits a gradient structure from amorphous phase to HA crystal.

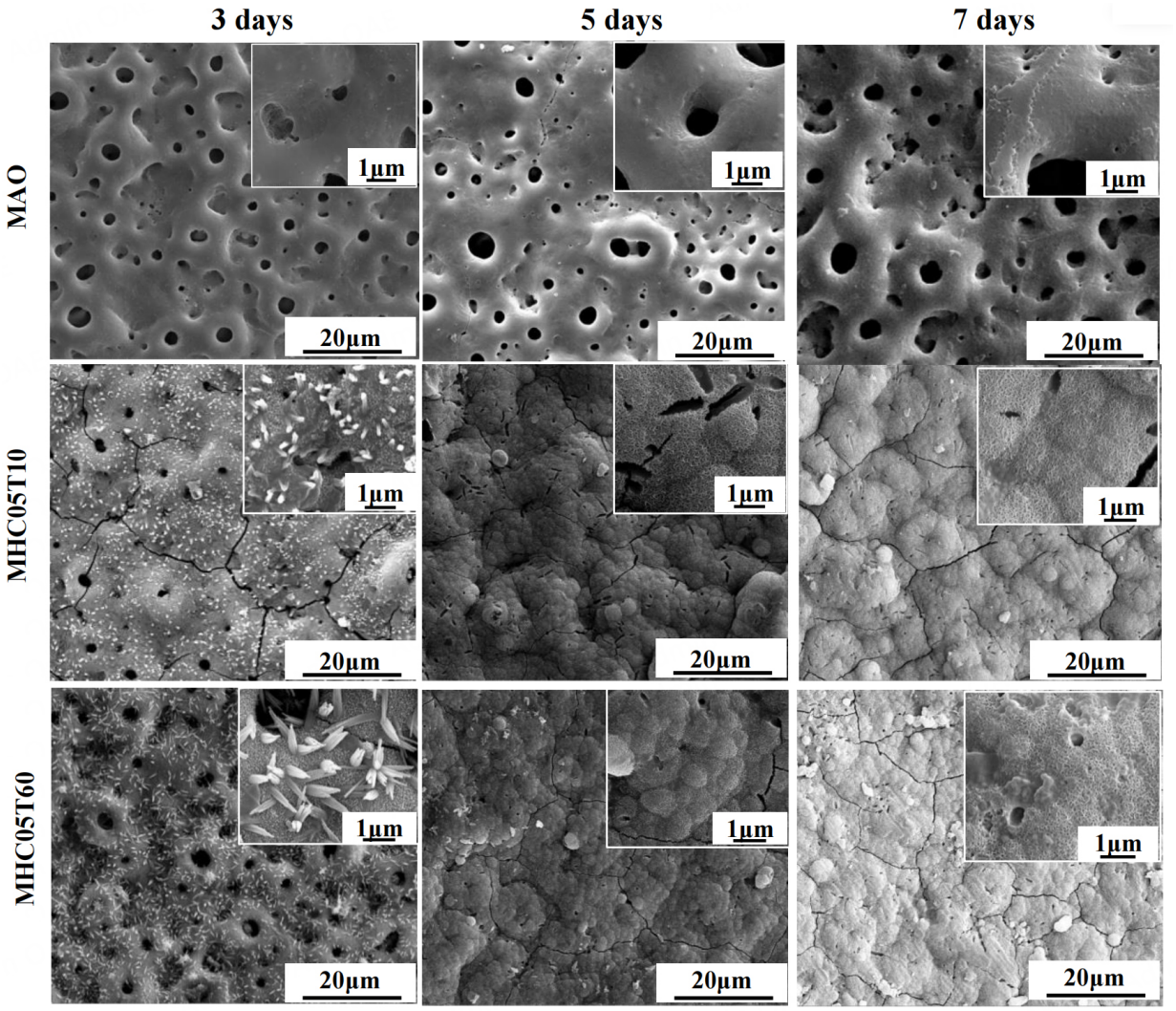

Figure 5. SEM micrographs for MAO, MHC05T10 and MHC05T60 samples after SBF soaking for 3,5 and 7 days.

In vitro bioactivity of MAO, MHC05T10, and MHC05T60 samples

SEM observation analysis

The *in vitro* mineralization abilities of the MAO, MHC05T10, and MHC05T60 samples were investigated, as shown in Figure 5. After SBF immersion, the MAO sample shows no significant change and remains similar to its original morphology, indicating poor bioactivity. In contrast, the MHC05T10 and MHC05T60 samples exhibit deposition of sol-gel films on their surfaces after 3 days of SBF soaking, along with noticeable changes in the initially formed HA submicron pillars, suggesting that transformation of these pillars occurs during soaking. After 5 and 7 days of immersion, pronounced apatite coatings are formed on the surfaces of both the MHC05T10 and MHC05T60 samples.

XRD and EDS analysis

Figure 6 illustrates the XRD patterns and EDS results of MAO, MHC05T10, and MHC05T60 coatings after 7 days of SBF soaking. In Figure 6A, the XRD patterns show that a new broad diffraction peak appears at $2\theta = 32°$ for MHC05T10 and MHC05T60 samples, which corresponds to the characteristic diffraction peaks of apatite, indicating that the deposited crystals on the coating surface are in the apatite phase. The MHC05T60 coating exhibits enhanced apatite formation ability, likely due to its higher initial HA content

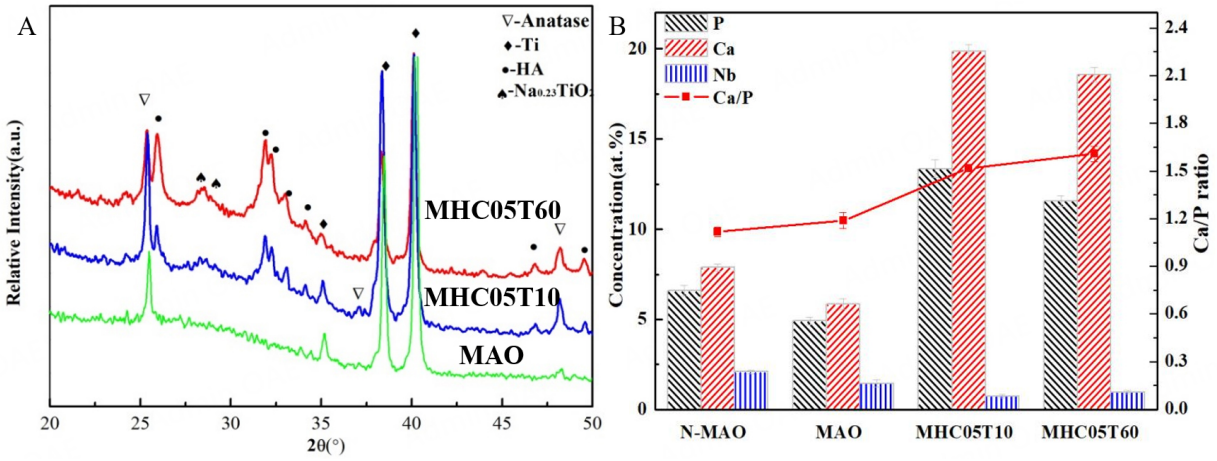

Figure 6. XRD patterns and EDS results of MAO, MHC05T10 and MHC05T60 samples after SBF immersion for 7 days: (A) XRD pattern; (B) EDS results, the error bars in (B) represent standard deviation (SD). Note: N-MAO refers the MAO sample without SBF immersion.

before SBF immersion. Figure 6B shows that after 7 days of SBF soaking, the Ca/P ratio of the MAO sample before and after soaking shows no obvious change, indicating that almost no apatite deposition occurs, which is consistent with the SEM results. The Ca/P ratios of the MHC05T10 and MHC05T60 samples are about 1.6 and 1.7, respectively, which are close to the Ca/P ratio of natural bone apatite, further confirming that the surface deposits are apatite.

Corrosion behavior of MAO and Nb-incorporated MAO coating

Figure 7 shows the potentiodynamic polarization curves and electrochemical impedance spectra (EIS) of the MAO and MAO-Nb samples in 0.5 mol/L NaOH solution, and the results are summarized in Table 3. In Figure 7A, the corrosion potential (E_{corr}) of the MAO-Nb sample (-0.280 ± 0.014 V) is slightly lower than that of the MAO sample (-0.250 ± 0.0125 V), and the corrosion current density (I_{corr}) of the MAO-Nb sample ((5.64 ± 0.082) × 10^{-9} A/cm²) is much lower than that of the MAO sample ((2.28 ± 0.035) × 10^{-8} A/cm²). Furthermore, the polarization resistance (R_p) of the MAO-Nb sample ((7.09 ± 0.38) × 10^6 Ω·cm²) is more than four times that of the MAO sample ((1.81 ± 0.21) × 10^6 Ω·cm²), indicating that Nb doping significantly improves the corrosion resistance of the MAO coating.

The EIS test results [Figures 7B and C] are consistent with the polarization curve results. The Nyquist plots of the MAO-Nb coating show a larger capacitive arc radius (about 1,500 kΩ·cm²) than that of the MAO coating (about 750 kΩ·cm²), indicating that the MAO-Nb coating has higher charge-transfer resistance and a lower corrosion rate. Figure 7C shows the Bode modulus plots of MAO and MAO-Nb coatings. Previous corrosion studies indicate that the impedance modulus at low frequency can represent the polarization resistance[40,41]. Therefore, the impedance modulus values at a frequency of 0.01 Hz can be considered as the polarization resistance (R_p). In this study, the impedance modulus value of MAO-Nb at 0.01 Hz (6.5 × 10^6 Ω·cm²) is slightly higher than that of the MAO coating (6.25 × 10^6 Ω·cm²), which further confirms that Nb doping improves the corrosion resistance of the MAO coating.

In vitro antibacterial ability of MAO and MHC05T60 coating

Figure 8 presents the colony-counting results and SEM images of the MAO and MHC05T60 samples against *E. coli* and *S. aureus*. In Figure 8A, the colony-counting results show that the number of viable bacteria on the MHC05T60 sample is significantly lower than that on the MAO sample. Based on these results, the antibacterial rates for *S. aureus* and *E. coli* on the MHC05T60 sample reach 96.1% and 87.3%, respectively, whereas those on the MAO coating are only 31.9% and 26.8%, respectively, indicating that the MH-treated Nb-doped MAO coating exhibits excellent broad-spectrum antibacterial performance.

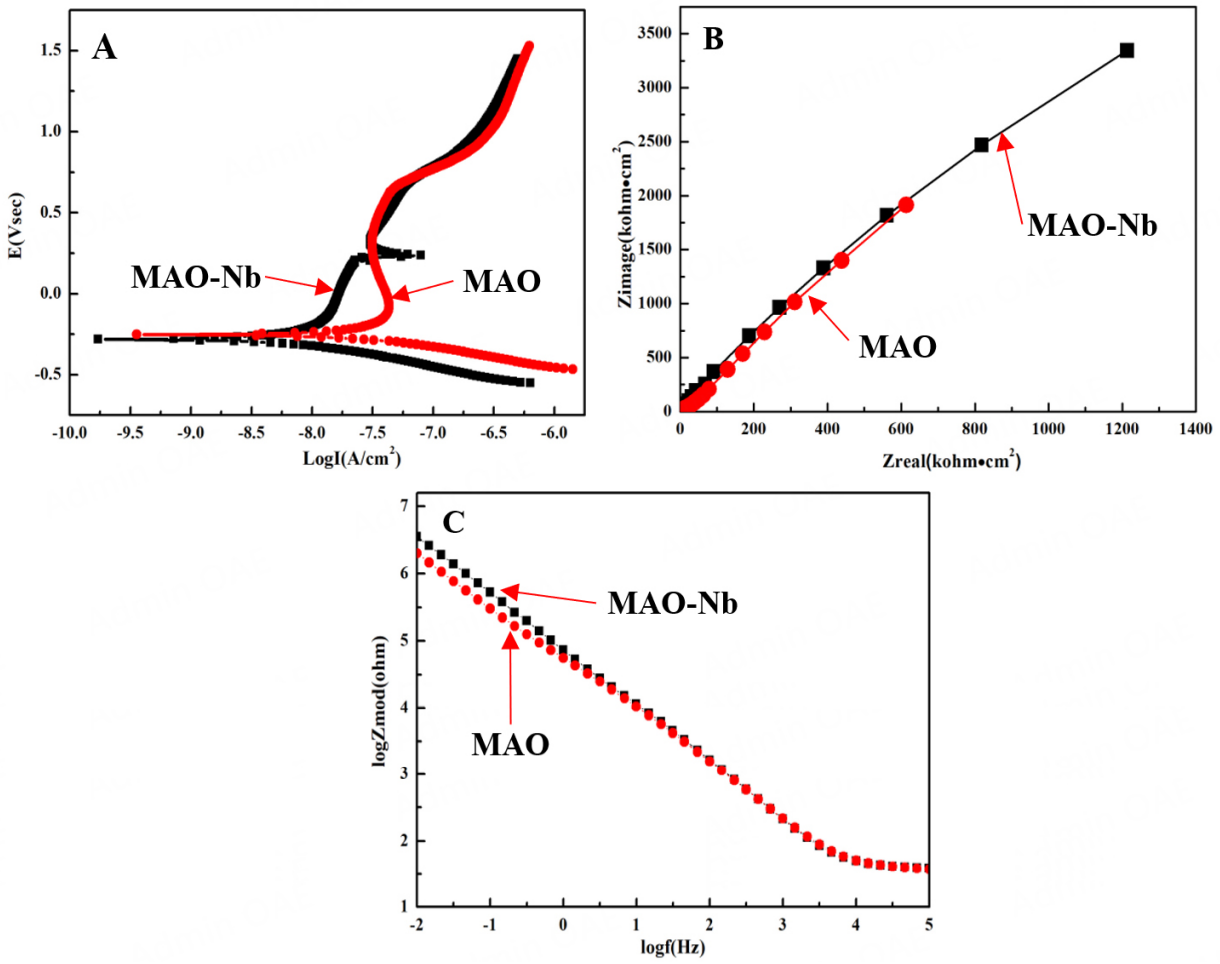

Figure 7. Potentiodynamic polarization curves and electrochemical impendence spectra (EIS) of MAO and MAO-Nb samples in 0.5 mol/L NaOH solution: (A) Potentiodynamic polarization curves; (B) Nyquist plots; (C) Bode modulus plots.

Table 3. Polarization parameters derived from the polarization curves in Figure 7A

Sample	E_{corr} (V *vs.* SCE)	I_{corr} (A•cm²)	β_a (V/decade)	β_c (V/decade)	R_p (Ω•cm²)
MAO	-0.250 ± 0.0125	(2.28 ± 0.035) × 10^{-8}	0.435	-0.121	(1.81 ± 0.21) × 10^{6}
MAO-Nb	-0.280 ± 0.014	(5.64 ± 0.082) × 10^{-9}	0.332	-0.127	(7.09 ± 0.38) × 10^{6}

MAO: Micro arc oxidized coating.

As shown in Figure 8B, *E. coli* and *S. aureus* adhered to the MAO coating remain in a normal proliferative state with intact cell morphology. In contrast, after MH treatment, the number of adhered bacteria on the MHC05T60 sample is very low, and the remaining bacteria exhibit clear cell damage, with several deformed and lysed cells, which directly confirms the excellent antibacterial effect of the MHC05T60 sample.

In vivo osseointegration of MAO and MHC05T60 coating

X-ray image observation

The X-ray images of the implant-bone complex at 4 and 8 weeks after implantation are shown in Figure 9. The axial and sagittal X-ray images show that no obvious gap, bone resorption, or implant loosening is observed at the bone-implant interface in either the MAO or MHC05T60 samples, indicating that both coatings exhibit good biocompatibility.

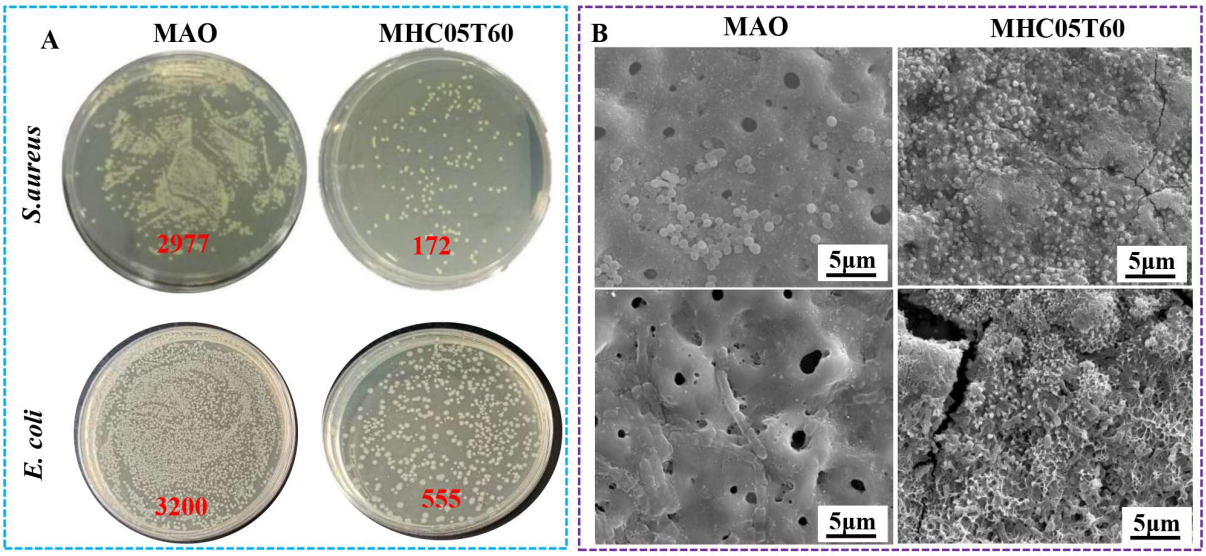

Figure 8. Optical images (A) and SEM images (B) of *E.coli* and *S.aureus* on the MAO and MHC05T60 samples.

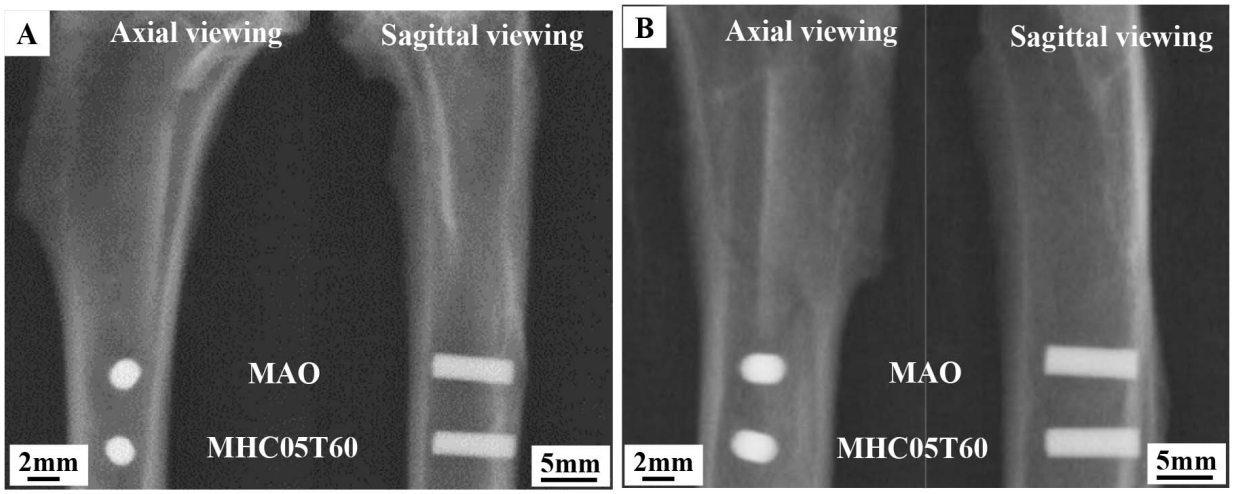

Figure 9. X-ray images of MAO and MHC05T60 implants in the tibia after healing for 4 and 8 weeks: (A) 4 weeks; (B) 8 weeks.

Micro-CT observation analysis

Figure 10 presents the micro-CT three-dimensional color images and statistical analyses of the MAO and MHC05T60 bone-implant complexes after 4 and 8 weeks of healing. The three-dimensional color images (green for bone tissue, red for soft tissue, and yellow for implant) show that bone formation around the MAO implant at 4 weeks after implantation is limited, and the newly formed bone is discontinuous and heterogeneous with low density. At 8 weeks after implantation, the new bone around the MAO implant becomes more continuous, and its density increases; however, a small amount of soft tissue remains at the interface. In contrast, the MHC05T60 implant exhibits a large amount of continuous and homogeneous bone tissue at 4 weeks after implantation, and the newly formed bone is closely attached to the implant surface. At 8 weeks after implantation, the new bone around the MHC05T60 implant becomes more mature, the bone volume is significantly increased, and the soft tissue at the interface is almost completely replaced by new bone.

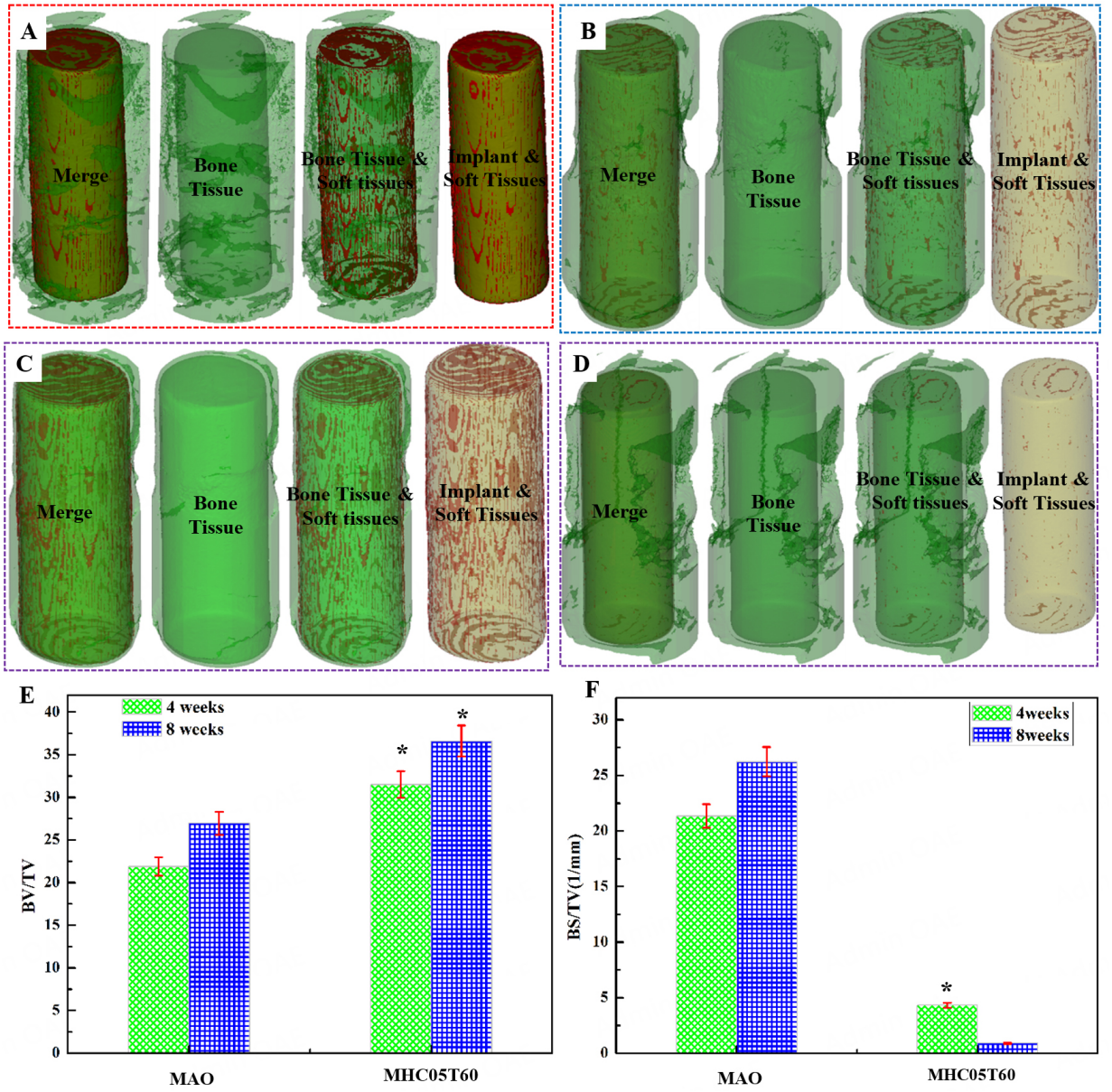

Figure 10. Micro-CT 3D color images and Statistical analysis for the MAO and MHC05T60 implant-bone complex at 4 and 8 weeks after implantation. (A and B) Micro-CT 3D color images for MAO implant-bone complex for 4 and 8 weeks; (C and D) Micro-CT 3D color images for MHC05T60 implant-bone complex for 4 and 8 weeks; (E) BV/TV; (F) BS/TV. Note: TV refers total volume of the tissues; BV refers biological tissue volume; BS refers the biological tissue surface area. *$P < 0.05$ compared to the MAO implant.

The quantitative analysis results [Figures 10E and F] show that the BV/TV value of the MAO implant at 4 weeks is about 22% and increases to 27% at 8 weeks. The BV/TV value of the MHC05T60 implant at 4 weeks is about 31.2%, which is higher than that of the MAO implant at 8 weeks, and increases to 37.5%, which is significantly higher than that of the MAO implant ($P < 0.05$). The BS/TV value of the MHC05T60 implant is lower than that of the MAO implant at the same time point, indicating that the new bone around the MHC05T60 implant is more mature and exhibits an improved bone structure. These micro-CT results confirm that the MHC05T60 coating significantly accelerates in vivo new bone formation and improves bone-implant osseointegration efficiency.

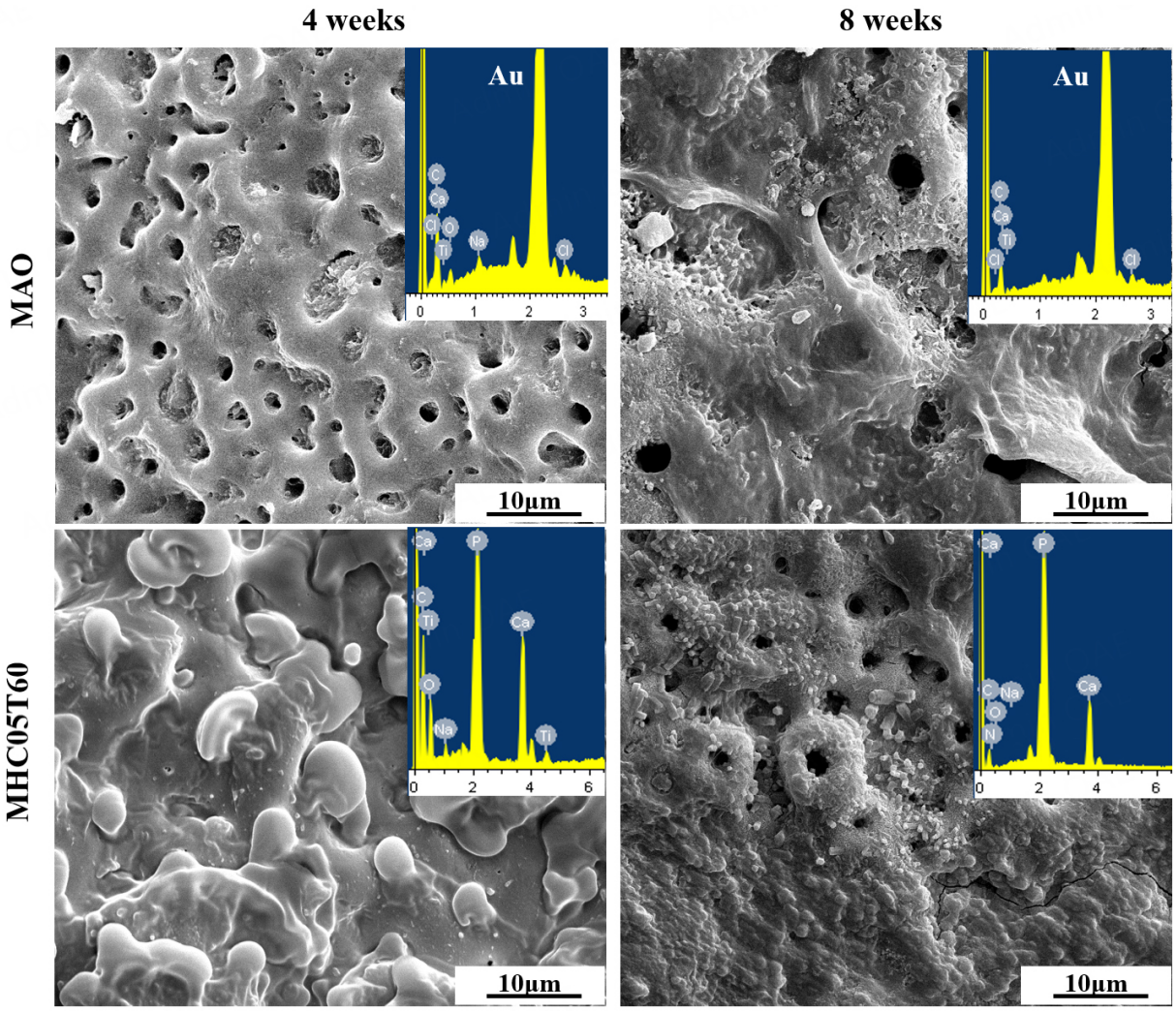

Figure 11. SEM images and corresponded EDS spectra of the taken-out MAO and MHC05T60 implants from the tibia after implantation for 4 and 8 weeks.

SEM observation of the bone-implant interface

Figure 11 presents SEM micrographs and corresponding EDS analyses of MAO and MHC05T60 implants extracted from the tibiae after 4 and 8 weeks of healing. At 4 weeks after implantation, a small amount of bone-like tissue is observed in the pore regions of the MAO implant, and the interface bonding is weak; some bone tissue is detached during the separation process, and the EDS spectrum shows a high C content. At 8 weeks after implantation, the amount of bone-like tissue on the MAO surface increases, but the main component at the interface remains soft tissue.

In contrast, a large number of bone-like deposits are observed on the surface of the MHC05T60 implant at 4 weeks after implantation, and the bone-implant interface is tightly bonded; fracture occurs in the bone tissue rather than at the interface during separation, and the EDS spectrum shows high Ca and P contents. At 8 weeks after implantation, the bone-like tissue on the MHC05T60 implant surface is further mineralized, and the Ca and P contents at the interface are close to those of natural bone, indicating the formation of a stable bone-bonding interface.

To avoid the influence of the coating on the analysis of the bone-implant interface status of MAO and MHC05T60 implants, SEM images of the tibia at the cortical bone position after implant removal for both

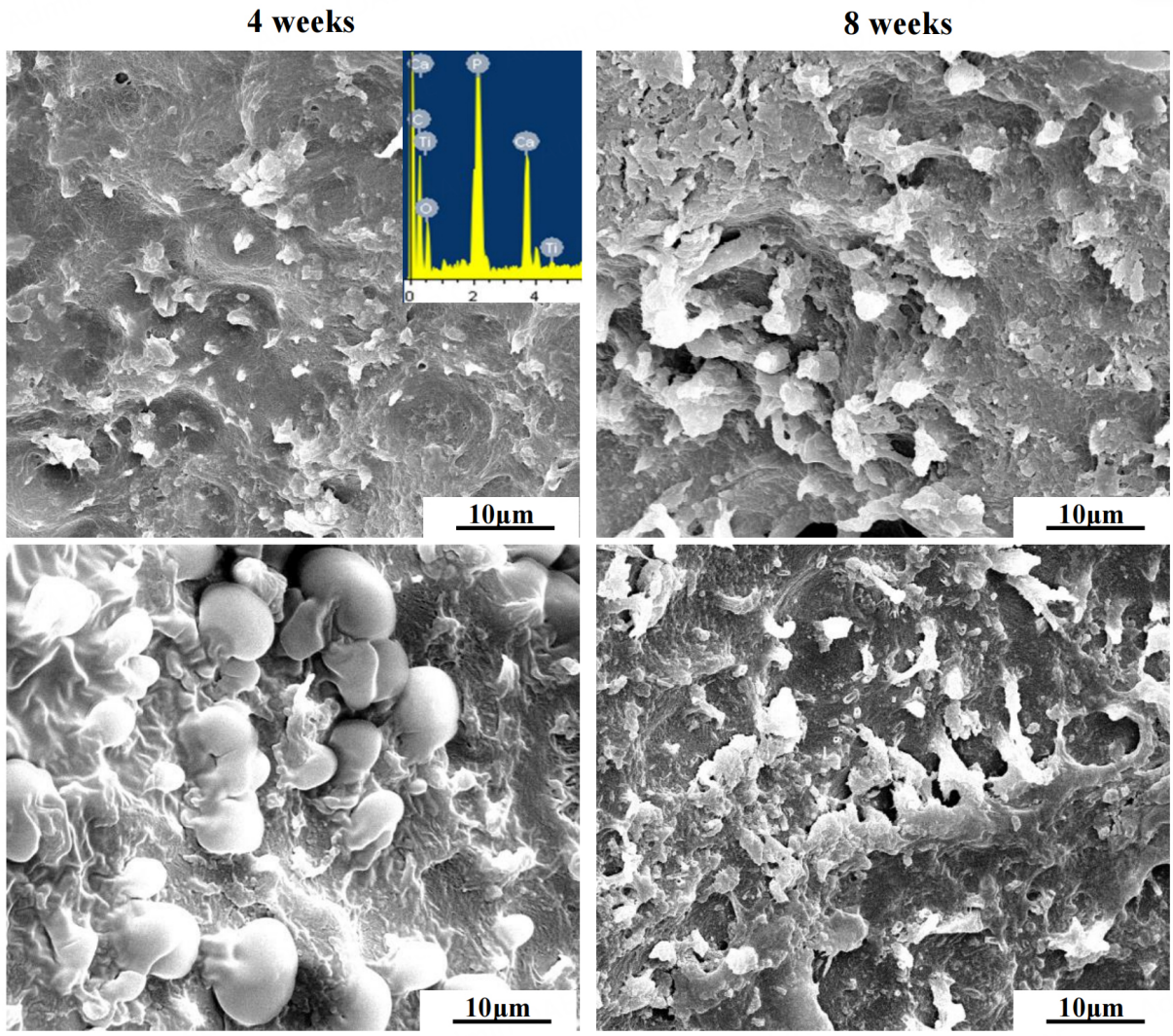

Figure 12. SEM images of the tibia at the cortical bone position after removing MAO and MHC05T60 implants after implantation for 4 and 8 weeks.

MAO and MHC05T60 samples are shown in Figure 12. At 4 weeks after implantation, numerous convex structures are observed in the tibia at the fracture site, corresponding to the original porous structure of the MAO sample. These convex structures are fragmented, and trace amounts of Ti are detected in this region, indicating that bone tissue has grown into the micropores and can withstand a certain load. At 8 weeks after implantation, the convex structures become larger, indicating that the amount of newly formed bone tissue increases. In contrast, numerous spherical mineral deposits are observed on the bone surface of the MHC05T60 implant at 4 weeks after implantation, consistent with the residual structure of the MHC05T60 implant surface, suggesting that fracture occurs on the bone side. At 8 weeks after implantation, the bone surface of the MHC05T60 implant forms a composite structure of convex residual coating and newly formed bone tissue, indicating that the MHC05T60 implant forms a firm and stable osseointegration interface with the surrounding bone tissue.

DISCUSSION

Formation of the multilayer coating with rod-like HA crystals

MH treatment is a novel and efficient surface modification technique that introduces a microwave field into the conventional hydrothermal process. Its unique heating characteristics, such as volumetric heating, rapid

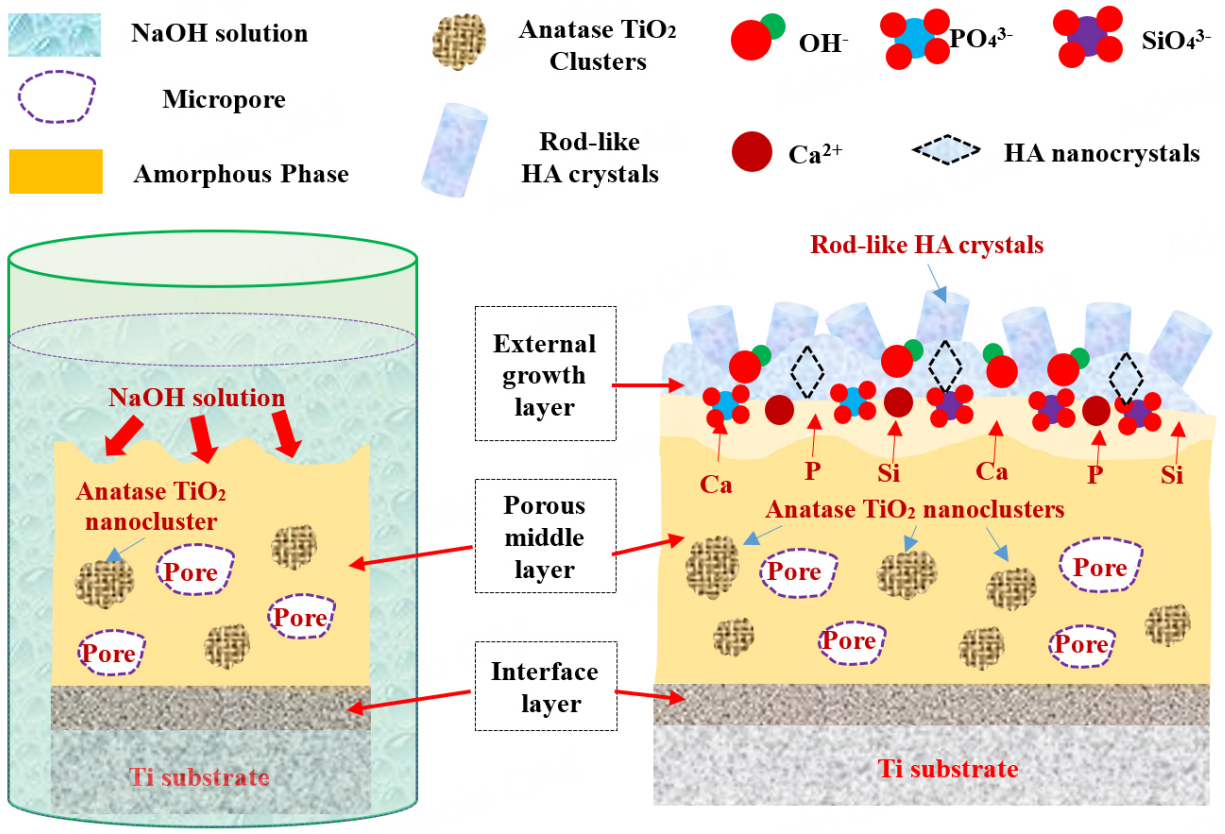

Figure 13. The schematic representation for the microstructure evolution and the formation of rod-like HA crystals.

heat transfer, and selective heating, enable rapid formation of HA crystals on the MAO coating surface. In this study, Nb was doped into the MAO coating by adding $C_{10}H_5NbO_{20}$ to the electrolyte, and MH treatment was conducted in NaOH solution to induce the formation of HA crystals. The formation mechanism of the three-layer structure of the MHC05T60 coating and the evolution of HA crystals are shown in Figure 13.

Based on the TEM results, the Nb-doped MAO coating is mainly composed of an amorphous structure containing Ca, P, Si, Na, and Nb elements, along with a small amount of anatase TiO_2 nanocrystal clusters, and its microstructure is similar to that reported in previous studies[29-31]. During MH treatment, the microwave field acts as a heat source and rapidly heats the NaOH solution to the target temperature (200 °C), forming a high-temperature and high-pressure reaction environment in a specialized autoclave. Under these conditions, the incorporated Ca, P, and Si elements diffuse toward the coating surface, resulting in the formation of SiO_4^{4-}, Ca^{2+}, and PO_4^{3-} species at the solution-coating interface. Hydroxide ions (OH^-) in the MH treatment solution facilitate HA nucleation by interacting with these species. The Si element in the coating forms SiO_4^{4-} at the interface, which acts as a heterogeneous nucleation site for HA crystals and promotes rapid nucleation. As the MH treatment time increases, HA nuclei are rapidly formed on the surface and subsequently grow *in situ* toward the solution, thereby forming a three-layer structure of the MHC05T60 sample, including an outer growth layer with rod-like HA crystals, a porous middle layer containing an amorphous structure and numerous TiO_2 nanocrystal clusters, and a dense interface layer.

Due to the interconnected porous structure of the MAO coating, some HA crystals are formed on the surfaces of internal pores. However, owing to the limitations imposed by the porous structure, only a limited amount of OH^- ions can diffuse into these pores, resulting in the formation of HA nuclei on the pore surfaces. Furthermore, the HA crystals observed in this study exhibit a short rod-like morphology, which

differs from the nanowire structures with smaller diameters and greater lengths formed on the surface of MH-treated MAO coatings without Nb, as previously reported[29-31]. Nb incorporated into the coating plays a key role in regulating the morphology of HA crystals. The Nb-doped MAO coating exhibits enhanced corrosion resistance in NaOH solution, suggesting a reduced reaction rate between OH^- and the MAO coating, which weakens the Ca and P concentration gradient at the coating-solution interface. As a result, fewer HA nuclei are formed on the Nb-incorporated MAO coating within a short time compared to the Nb-free MAO coating. Consequently, the formation of finer and longer HA crystals on the Nb-doped MAO coating is less favorable due to the insufficient Ca and P concentration gradient. In contrast, short rod-like HA crystals with larger diameters are formed, which may be more favorable for inducing bone formation, as this morphology resembles HA crystals in natural bone.

Biological performance of MAO and MHC05T60 coatings

Antibacterial ability of MAO and MHC05T60 coatings

The *in vitro* antibacterial test results show that the MHC05T60 sample exhibits excellent broad-spectrum antibacterial performance against *E. coli* and *S. aureus*. The colony-counting results and SEM images demonstrate that the antibacterial capability of the MAO coating is significantly enhanced after MH treatment. The adhesion and proliferation of *E. coli* and *S. aureus* on the surface of the MHC05T60 sample are markedly inhibited, thereby reducing the risk of post-implantation infection. These findings indicate that MH treatment can effectively improve the antibacterial properties of MAO coatings and provide a feasible approach for enhancing antibacterial performance.

Several factors, including surface roughness[42-44], surface topology[42-44], and chemical composition[20,42-44], may influence the antibacterial ability of the MHC05T60 sample. The MAO coating exhibits a relatively smooth porous topological structure, allowing *E. coli* and *S. aureus* to easily adhere to its surface, as confirmed by the SEM images in Figure 8B. In contrast, the adhered bacterial structures on the MHC05T60 sample are significantly damaged, suggesting that the nanoscale microstructure positively affects antibacterial performance. This observation indicates that surface morphology plays an important role in regulating bacterial adhesion and proliferation. Previous studies have also demonstrated that surface morphology can influence bacterial adhesion and proliferation[20].

Additionally, the chemical composition of the MHC05T60 sample influences the adhesion and proliferation of *E. coli* and *S. aureus*. Following MH treatment, the concentrations of Ca and P elements on the surface of the MHC05T60 sample increase due to the formation of HA crystals. Previous studies indicate that Ca and P elements can affect bacterial adhesion and proliferation[20]. During the bacterial culture process, the MHC05T60 coating releases higher levels of Ca and P due to the dissolution of rod-like HA crystals. The amorphous Nb_2O_5 in the MHC05T60 sample can induce the generation of reactive oxygen species (ROS), such as H_2O_2, O_2^{2-}, and OH^-, thereby further inhibiting bacterial growth[45]. Released Nb^{5+} from Nb_2O_5 can penetrate bacterial cells by disrupting the cell wall and damaging DNA and RNA, thereby inhibiting bacterial proliferation, similar to the mechanism of Zn^{2+}[46]. Therefore, the enhanced antibacterial ability of the modified MAO coating results from the combined effects of incorporated elements and the porous surface topology.

In vitro and in vivo bioactivity of MAO and MHC05T60 coatings

The formation of apatite is considered an important process in new bone formation around the implant. *In vitro* SBF soaking is an effective method to evaluate the bioactivity of materials[47,48]. The SBF soaking experiments and *in vivo* animal studies confirm that the MHC05T60 coating exhibits excellent *in vitro* bioactivity and *in vivo* osseointegration performance. This enhancement is mainly attributed to the synergistic effect of short rod-like HA crystals and Nb doping, and can be explained by two main factors.

First, the rod-like HA crystals exhibit good crystallographic compatibility with apatite, acting as heterogeneous nucleation sites for apatite and significantly accelerating apatite deposition. Second, the Nb-doped HA crystals exhibit good solubility, similar to the effects of Sr, F, and Si ions[49,50]. Consequently, during SBF immersion, dissolution of Nb-substituted HA crystals increases the local concentrations of Ca^{2+} and PO_4^{3-} ions at the outermost layer of the MHC05T60 sample. These factors collectively indicate that the MHC05T60 coating with numerous rod-like HA crystals possesses excellent apatite-inducing ability.

The *in vivo* osseointegration behavior in the tibia is a complex process involving deposition of bone-like apatite, fluid-material exchange, and formation of new biological tissues[51]. X-ray and micro-CT three-dimensional color images indicate excellent biocompatibility of all implants *in vivo*. Furthermore, the bone-implant interface cannot be clearly identified from these images. Therefore, SEM images of both the implant and tibia sides were used to investigate the interface status. The fracture position indicates a favorable interface between the bone and the MHC05T60 implant, as confirmed by the SEM images in Figures 11 and 12. The fracture SEM images demonstrate that the MHC05T60 implant exhibits excellent osseointegration performance, which is attributed to its micro/nano dual-scale porous surface with numerous rod-like HA crystals, as further supported by the push-out force shown in Supplementary Figure 1. As reported in related literature and previous studies, a micro/nano dual-scale porous surface with HA nanowires has been achieved through combined techniques of MAO/HT[22,23,52-54], MAO/MH[30,31], and MAO/MSH[29], which is similar to the microstructure observed in this study. The variation in microstructure is mainly attributed to the improved corrosion resistance of the MAO-Nb coating. To evaluate differences in *in vivo* osseointegration, the bone-implant extraction force was summarized and compared, as shown in Supplementary Table 1. Overall, the MH-treated MAO-Nb coating with a micro/nano dual-scale porous surface and rod-like HA crystals presents a promising material for bone repair applications.

CONCLUSION

The incorporation of Nb, MAO, and MH treatment was used to rapidly construct a micro/nano dual-scale porous surface with numerous rod-like HA crystals on the Ti surface. The MHC05T60 coating consists of an outer growth layer with numerous rod-like HA crystals, a porous middle layer containing numerous anatase TiO_2 clusters and an amorphous structure, and a dense interface layer. Furthermore, the incorporation of Nb promotes the formation of HA with a uniform submicron pillar-like morphology, which is attributed to enhanced corrosion resistance of the MAO coating. Based on the results of *in vitro* antibacterial tests, SBF immersion tests, and *in vivo* animal experiments, the MHC05T60 sample demonstrates excellent overall biological performance, including superior antibacterial ability, good apatite deposition capacity, and outstanding *in vivo* bone-inducing ability. The enhancement of these properties is attributed to the micro/nano dual-scale rough porous surface and the specific elemental composition of the rod-like HA crystals. Consequently, the MH-treated Nb-incorporated MAO coating presents a promising alternative material for bone-related applications.

DECLARATIONS

Authors' contribution

Writing-review and editing, writing-initial draft, visualization, methodology, investigation, data processing: Wei, D.

Writing-review and editing, supervision, data processing, visualization: Du, Q.

Writing-review and editing, supervision, conceptualization, investigation, writing-comment and editing: Petrov, Y. V.

Data collection, experimental operations, technical support: Wang, Q.

Experimental technical support, data collection, preliminary analysis: Cheng, S.

Experimental implementation and technical support: Wang, Y.

All authors have reviewed and approved the final version of the manuscript

Availability of data and materials

The author declares that data supporting the results of this study can be obtained in the paper and its Supplementary Materials. If other formats of raw data files are required, they can be obtained from the corresponding authors upon reasonable request. In addition, this article also provides raw data for further verification and research.

AI and AI-assisted tools statement

During the preparation of this manuscript, the AI tool Chat AI(version 1.7.1, released 2022-11-30) was used solely for language editing. The tool did not influence the study design, data collection, analysis, interpretation, or the scientific content of the work. All authors take full responsibility for the accuracy, integrity, and final content of the manuscript.

Financial support and sponsorship

This study received substantial support from the following organizations: National Natural Science Foundation of China (Grant No. 52101284), Young Talents of Basic Research in Universities of Heilongjiang Province (YQJH2023246), Fundamental Research Foundation for Universities of Heilongjiang Province (2023-KYYWF-0119), Heilongjiang Province Postdoctoral Funding (LBH-Z23129, LBH-TZ2409), National Natural Science Foundation of China (Grant No. U22A20315) for this study.

Conflicts of interest

All authors declared that there are no conflicts of interest.

Ethical approval and consent to participate

The tibial implantation model was covered by the approved animal protocol (IACUC No. 2020127).

Consent for publication

Not applicable.

Supplementary Materials

Supplementary Materials

REFERENCES

1. Sun, X.; Liu, T.; Wang, Q.; Zhang, J.; Cao, M. Surface modification and functionalities for titanium dental implants. *ACS. Biomater. Sci. Eng.* **2023**, *9*, 4442-61. DOI PubMed
2. Abd-Elaziem, W.; Darwish, M. A.; Hamada, A.; Daoush, W. M. Titanium-based alloys and composites for orthopedic implants applications: a comprehensive review. *Mater. Des.* **2024**, *241*, 112850. DOI
3. Li, Y.; Pan, Q.; Xu, J.; et al. Overview of methods for enhancing bone regeneration in distraction osteogenesis: potential roles of biometals. *J. Orthop. Transl.* **2021**, *27*, 110-8. DOI PubMed PMC
4. Azmat, A.; Asrar, S.; Channa, I. A.; et al. Comparative study of biocompatible titanium alloys containing non-toxic elements for orthopedic implants. *Crystals* **2023**, *13*, 467. DOI
5. Hwang, H.; Park, J.; Lee, D. Effect of molybdenum content on microstructure and mechanical properties of Ti-Mo-Fe alloys by powder metallurgy. *Appl. Sci.* **2022**, *12*, 7257. DOI
6. Dela Cruz, M. L.; Yakubov, V.; Li, X.; Ferry, M. Microstructure evolution in laser powder bed fusion-built Fe-Mn-Si shape memory alloy. *Microstructures* **2023**, *3*, 2023012. DOI
7. Lv, J.; Cheng, Y. Amorphous coatings on tantalum formed by plasma electrolytic oxidation in aluminate electrolyte and high temperature crystallization treatment. *Surf. Coat. Technol.* **2022**, *434*, 128171. DOI
8. Davis, R.; Singh, A.; Jackson, M. J.; et al. A comprehensive review on metallic implant biomaterials and their subtractive manufacturing. *Int. J. Adv. Manuf. Technol.* **2022**, *120*, 1473-530. DOI PubMed PMC

9. Si, C. R.; Duan, B. B.; Zhang, Q.; Cai, J.; Wu, W. Microstructure, corrosion-resistance, and wear-resistance properties of subsonic flame sprayed amorphous Fe-Mo-Cr-Co coating with extremely high amorphous rate. *J. Mater. Res. Technol.* **2020**, *9*, 3292-303. DOI
10. Koju, N.; Niraula, S.; Fotovvati, B. Additively manufactured porous Ti6Al4V for bone implants: a review. *Metals* **2022**, *12*, 687. DOI
11. Garrido, B.; Garcia-Giralt, N.; Rodríguez, M. A.; De Aza, A. H.; Cano, I. G. Bioactive glasses as alternatives to hydroxyapatite for bone implant coatings: a comparative study. *J. Biomed. Mater. Res.* **2025**, *113*, e35577. DOI
12. Singh, G.; Sharma, S.; Mittal, M.; et al. Impact of post-heat-treatment on the surface-roughness, residual stresses, and micromorphology characteristics of plasma-sprayed pure hydroxyapatite and 7%-Aloxite reinforced hydroxyapatite coatings deposited on titanium alloy-based biomedical implants. *J. Mater. Res. Technol.* **2022**, *18*, 1358-80. DOI
13. Hao, X.; Liu, H.; Zhang, X.; et al. Friction-wear behaviors and microstructure of AlTiVCrNb lightweight refractory high-entropy alloy coating prepared by laser cladding on Ti-6Al-4V substrate. *J. Mater. Res. Technol.* **2024**, *29*, 1-11. DOI
14. El Garah, M.; Touaibia, D. E.; Achache, S.; et al. Effect of nitrogen content on structural and mechanical properties of AlTiZrTaHf(-N) high entropy films deposited by reactive magnetron sputtering. *Surf. Coat. Technol.* **2022**, *432*, 128051. DOI
15. Patel, R. Periprosthetic joint infection. *N. Engl. J. Med.* **2023**, *388*, 251-62. DOI
16. Ayalew, A. A.; Han, X.; Sakairi, M. A critical review of additive material manufacturing through electrochemical deposition techniques. *Addit. Manuf.* **2023**, *77*, 103796. DOI
17. Zhou, J.; Li, B.; Lu, S.; Zhang, L.; Han, Y. Regulation of osteoblast proliferation and differentiation by interrod spacing of Sr-HA nanorods on microporous titania coatings. *ACS. Appl. Mater. Interfaces.* **2013**, *5*, 5358-65. DOI
18. Shimabukuro, M.; Tsutsumi, H.; Tsutsumi, Y.; et al. Enhancement of antibacterial property of titanium by two-step micro arc oxidation treatment. *Dent. Mater. J.* **2021**, *40*, 592-8. DOI
19. Li, G.; Ma, F.; Liu, P.; et al. Review of micro-arc oxidation of titanium alloys: Mechanism, properties and applications. *J. Alloys. Compd.* **2023**, *948*, 169773. DOI
20. Du, Q.; Wei, D.; Wang, Y.; et al. The effect of applied voltages on the structure, apatite-inducing ability and antibacterial ability of micro arc oxidation coating formed on titanium surface. *Bioact. Mater.* **2018**, *3*, 426-33. DOI PubMed PMC
21. Liu, F.; Song, Y.; Wang, F.; Shimizu, T.; Igarashi, K.; Zhao, L. Formation characterization of hydroxyapatite on titanium by microarc oxidation and hydrothermal treatment. *J. Biosci. Bioeng.* **2005**, *100*, 100-4. DOI
22. Zhou, J.; Li, B.; Han, Y.; Zhao, L. The osteogenic capacity of biomimetic hierarchical micropore/nanorod-patterned Sr-HA coatings with different interrod spacings. *Nanomed. Nanotechnol. Biol. Med.* **2016**, *12*, 1161-73. DOI
23. Zhou, J.; Han, Y. Effect of hydrothermal treatment model on the formation of Sr-HA nanorod arrays on microarc oxidized titania coatings. *Appl. Surf. Sci.* **2013**, *286*, 384-90. DOI
24. Mehta, A.; Singh, G. Consequences of hydroxyapatite doping using plasma spray to implant biomaterials: review paper. *J. Electrochem. Sci. Eng.* **2023**, *13*, 5-23. DOI
25. Kebriyaei, A.; Rahimipour, M. R.; Razavi, M.; Alizade Herfati, A. Effect of solution precursor on microstructure and high-temperature properties of the thermal barrier coating made by solution precursor plasma spray (SPPS) process. *J. Therm. Spray. Technol.* **2022**, *32*, 8-28. DOI
26. Nazir, A.; Gokcekaya, O.; Md Masum Billah, K.; et al. Multi-material additive manufacturing: a systematic review of design, properties, applications, challenges, and 3D printing of materials and cellular metamaterials. *Mater. Des.* **2023**, *226*, 111661. DOI
27. Fosca, M.; Streza, A.; Antoniac, I. V.; Vadalà, G.; Rau, J. V. Ion-doped calcium phosphate-based coatings with antibacterial properties. *J. Funct. Biomater.* **2023**, *14*, 250. DOI PubMed PMC
28. Wang, D.; Yue, Y.; Xie, Z.; et al. Chloride-induced depassivation and corrosion of mild steel in magnesium potassium phosphate cement. *Corros. Sci.* **2022**, *206*, 110482. DOI
29. Du, Q.; Wei, D.; Cheng, S.; et al. Rapid structural evolution and bone inducing mechanism of the multilayer coating with silicon-doped hydroxyapatite crystals on the microwave water steaming-hydrothermally treated titania coating. *Appl. Surf. Sci.* **2021**, *539*, 148153. DOI
30. Du, Q.; Wei, D.; Wang, S.; et al. TEM analysis and in vitro and in vivo biological performance of the hydroxyapatite crystals rapidly formed on the modified microarc oxidation coating using microwave hydrothermal technique. *Chem. Eng. J.* **2019**, *373*, 1091-110. DOI
31. Wei, D.; Du, Q.; Wang, S.; et al. Rapid fabrication, microstructure, and *in Vitro* and *in Vivo* investigations of a high-performance multilayer coating with external, flexible, and silicon-doped hydroxyapatite nanorods on titanium. *ACS. Biomater. Sci. Eng.* **2019**, *5*, 4244-62. DOI
32. Zhang, P.; Zhang, Z.; Li, W. Antibacterial TiO_2 coating incorporating silver nanoparticles by microarc oxidation and ion implantation. *J. Nanomater.* **2013**, *2013*, 542878. DOI
33. Zhou, R.; Zhou, Y.; Cheng, J.; et al. Surface configuration of microarc oxidized Ti with regionally loaded chitosan hydrogel containing ciprofloxacin for improving biological performance. *Mater. Today. Bio.* **2022**, *16*, 100380. DOI PubMed PMC

34. Wu, J.; Cheng, Y.; Zhao, X.; et al. Antibacterial activity and biological performance of a novel antibacterial coating containing a halogenated furanone compound loaded poly(L-lactic acid) nanoparticles on microarc-oxidized titanium. *Int. J. Nanomed.* **2015**, *2015*, 727-37. DOI
35. Yan, X.; Zhao, M.; Yang, Y.; et al. Improvement of biodegradable and antibacterial properties by solution treatment and micro-arc oxidation (MAO) of a magnesium alloy with a trace of copper. *Corros. Sci.* **2019**, *156*, 125-38. DOI
36. Zhang, X.; Li, C.; Yu, Y.; et al. Characterization and property of bifunctional Zn-incorporated TiO_2 micro-arc oxidation coatings: the influence of different Zn sources. *Ceram. Int.* **2019**, *45*, 19747-56. DOI
37. Zhang, Y. Y.; Zhu, Y.; Lu, D. Z.; et al. Evaluation of osteogenic and antibacterial properties of strontium/silver-containing porous TiO_2 coatings prepared by micro-arc oxidation. *J. Biomed. Mater. Res.* **2020**, *109*, 505-16. DOI
38. Oyane, A.; Kim, H. M.; Furuya, T.; Kokubo, T.; Miyazaki, T.; Nakamura, T. Preparation and assessment of revised simulated body fluids. *J. Biomed. Mater. Res.* **2003**, *65A*, 188-95. DOI
39. Du, Q.; Wei, D.; Liu, S.; et al. The hydrothermal treated Zn-incorporated titania based microarc oxidation coating: Surface characteristics, apatite-inducing ability and antibacterial ability. *Surf. Coat. Technol.* **2018**, *352*, 489-500. DOI
40. Nishikata, A.; Ichihara, Y.; Tsuru, T. An application of electrochemical impedance spectroscopy to atmospheric corrosion study. *Corros. Sci.* **1995**, *37*, 897-911. DOI
41. Kim, H.; Ikehara, Y.; Kim, J.; Hosoda, H.; Miyazaki, S. Martensitic transformation, shape memory effect and superelasticity of Ti-Nb binary alloys. *Acta. Mater.* **2006**, *54*, 2419-29. DOI
42. Soylu, H. M.; Chevallier, P.; Copes, F.; et al. A novel strategy to coat dopamine-functionalized titanium surfaces with agarose-based hydrogels for the controlled release of gentamicin. *Front. Cell. Infect. Microbiol.* **2021**, *11*, 678081. DOI PubMed PMC
43. Ciobanu, C. S.; Predoi, D.; Iconaru, S. L.; et al. New nanobioceramics based on hydroxyapatite for biomedical applications: stability and properties. *Nanomaterials* **2025**, *15*, 224. DOI PubMed PMC
44. Bharadishettar, N.; Bhat, K. U.; Bhat Panemangalore, D. Coating technologies for copper based antimicrobial active surfaces: a perspective review. *Metals* **2021**, *11*, 711. DOI
45. Raghupathi, K. R.; Koodali, R. T.; Manna, A. C. Size-dependent bacterial growth inhibition and mechanism of antibacterial activity of zinc oxide nanoparticles. *Langmuir* **2011**, *27*, 4020-8. DOI PubMed
46. Wang, G.; Jin, W.; Qasim, A. M.; et al. Antibacterial effects of titanium embedded with silver nanoparticles based on electron-transfer-induced reactive oxygen species. *Biomaterials* **2017**, *124*, 25-34. DOI
47. Kokubo, T.; Takadama, H. How useful is SBF in predicting in vivo bone bioactivity? *Biomaterials* **2006**, *27*, 2907-15. DOI PubMed
48. Kokubo, T.; Kushitani, H.; Sakka, S.; Kitsugi, T.; Yamamuro, T. Solutions able to reproduce *in vivo* surface-structure changes in bioactive glass-ceramic A-W[3]. *J. Biomed. Mater. Res.* **2004**, *24*, 721-34. DOI
49. Pietak, A. M.; Reid, J. W.; Stott, M. J.; Sayer, M. Silicon substitution in the calcium phosphate bioceramics. *Biomaterials* **2007**, *28*, 4023-32. DOI PubMed
50. Boanini, E.; Gazzano, M.; Bigi, A. Ionic substitutions in calcium phosphates synthesized at low temperature. *Acta. Biomater.* **2010**, *6*, 1882-94. DOI
51. Sheikh, Z.; Najeeb, S.; Khurshid, Z.; Verma, V.; Rashid, H.; Glogauer, M. Biodegradable materials for bone repair and tissue engineering applications. *Materials* **2015**, *8*, 5744-94. DOI PubMed PMC
52. Zhou, J.; Li, B.; Zhao, L.; Zhang, L.; Han, Y. F-Doped Micropore/Nanorod Hierarchically Patterned Coatings for Improving Antibacterial and Osteogenic Activities of Bone Implants in Bacteria-Infected Cases. *ACS. Biomater. Sci. Eng.* **2017**, *3*, 1437-50. DOI
53. Li, B.; Han, Y.; Li, M. Enhanced osteoblast differentiation and osseointegration of a bio-inspired HA nanorod patterned pore-sealed MgO bilayer coating on magnesium. *J. Mater. Chem. B.* **2016**, *4*, 683-93. DOI
54. Li, B.; Gao, P.; Zhang, H.; Guo, Z.; Zheng, Y.; Han, Y. Osteoimmunomodulation, osseointegration, and*in vivo*mechanical integrity of pure Mg coated with HA nanorod/pore-sealed MgO bilayer. *Biomater. Sci.* **2018**, *6*, 3202-18. DOI